energies

MDPI

Article

Three-Port Converter for Integrating Energy Storage and Wireless Power Transfer Systems in Future Residential Applications

Hyeon-Seok Lee [1] and Jae-Jung Yun [2,*]

[1] Department of Electrical Engineering, POSTECH, Pohang 37673, Korea; hsasdf@postech.ac.kr
[2] Department of Electronics and Electrical Engineering, Daegu University, Gyeongsan 38453, Korea
* Correspondence: jjyun@daegu.ac.kr; Tel.: +82-53-850-6612

Received: 15 November 2019; Accepted: 2 January 2020; Published: 5 January 2020

Abstract: This paper presents a highly efficient three-port converter to integrate energy storage (ES) and wireless power transfer (WPT) systems. The proposed converter consists of a bidirectional DC-DC converter and an AC-DC converter with a resonant capacitor. By sharing an inductor and four switches in the bidirectional DC-DC converter, the bidirectional DC-DC converter operates as a DC-DC converter for ES systems and simultaneously as a DC-AC converter for WPT systems. Here, four switches are turned on under the zero voltage switching conditions. The AC-DC converter for WPT system achieves high voltage gain by using a resonance between the resonant capacitor and the leakage inductance of a receiving coil. A 100-W prototype was built and tested to verify the effectiveness of the converter; it had a maximum power-conversion efficiency of 95.9% for the battery load and of 93.8% for the wireless charging load.

Keywords: energy storage system; wireless power transfer system; DC-DC power conversion; photovoltaic power system

1. Introduction

Photovoltaics (PVs) constitute a promising alternative energy source due to diverse applications and the ubiquity of sunlight [1–4]. Residential PV systems consist of a PV module and a PV inverter, and it converts sunlight into electricity. However, energy output by PV systems is not constant because it is affected by weather conditions and the day/night cycle. Therefore, energy storage (ES) systems are used to efficiently manage the PV energy. They consist of a battery and a bidirectional DC-DC converter that connects to the PV system [5–7]. Besides, in the near future, the wireless power transfer (WPT) systems will be widely used to wirelessly charge laptops as well as cell phones in many households [8–11]. Therefore, future PV energy delivery and management infrastructure for residential applications will consist of PV systems, ES systems, and WPT systems (Figure 1a).

Three-port converters have been used to reduce the cost and size of infrastructure, such as micro-grids and smart grids [12–18]. The infrastructure consists of several systems, so its cost and size increase in proportion to the number of systems. To alleviate this problem, two systems are integrated through on a three-port converter. The three-port converters usually add a port to a typical converter that has two ports, either by using a three-winding transformer instead of a two-winding transformer [13–15] or by using the storage capacitor in the typical converter as a third port [16–18].

Many three-port converters have been introduced to integrate renewable energy sources (e.g., PV, fuel cell, wind turbine) with ES systems, but a three-port converter to integrate ES and WPT systems has not been considered. Therefore, this paper presents a three-port converter that can integrate the ES and WPT systems that will be used in future PV energy delivery and management infrastructure

for residential applications (Figure 1b). The proposed three-port converter consists of a bidirectional DC-DC converter for an ES system and an AC-DC converter with a resonant capacitor. The bidirectional DC-DC converter can also operate as a DC-AC converter of the WPT system because the inductor in the bidirectional DC-DC converter is also used as a transmitting coil for a WPT system. With these few components, the proposed converter can store energy for the ES system and simultaneously transfer the energy by using a WPT system. The proposed converter has a high power-conversion efficiency by achieving zero voltage switching (ZVS) turn-on for switches, and has high voltage gain for WPT by using a resonance between a resonant capacitor and a leakage inductance of a receiving coil.

Section 2 describes the circuit structure and operating principles of the proposed converter. Section 3 presents experimental results, and Section 4 concludes the paper.

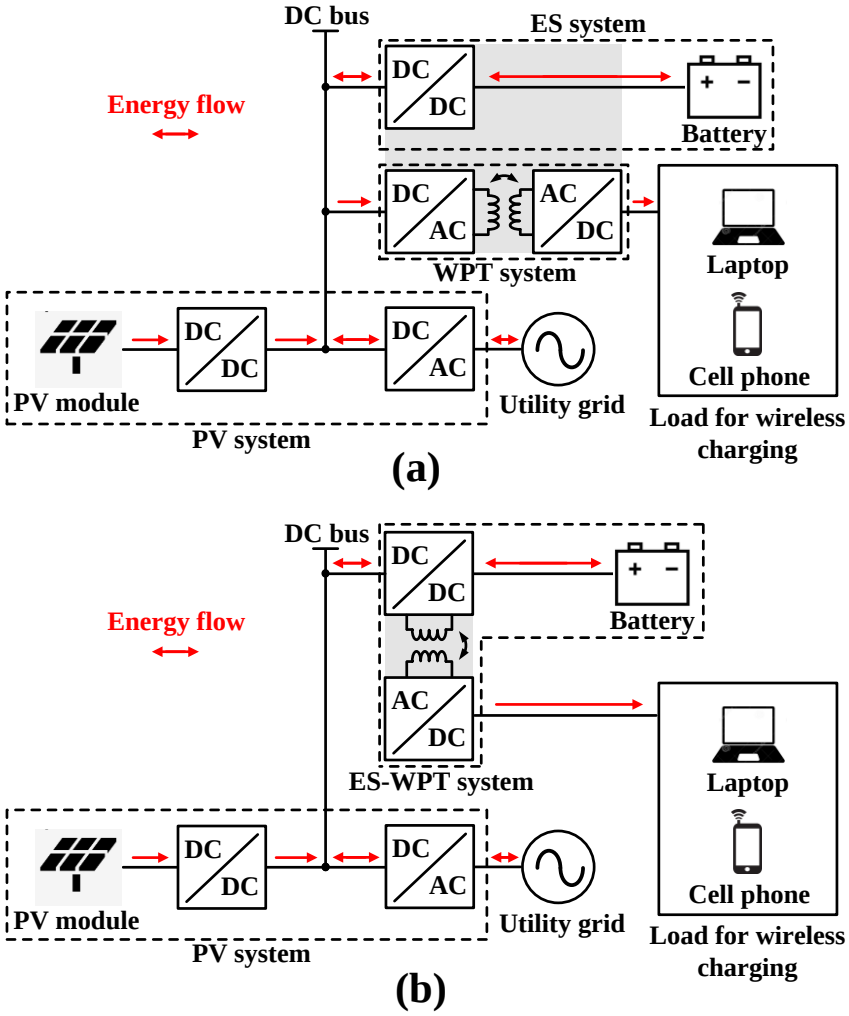

Figure 1. Future photovoltaic (PV) energy delivery and management infrastructure; (**a**) typical topology, (**b**) proposed topology.

2. Proposed Three-Port Converter

2.1. Circuit Structure

The proposed converter (Figure 2a) combines the structures of a bidirectional DC-DC converter and an AC-DC converter.

The bidirectional DC-DC converter is located between a DC bus and a battery to transfer the energy in both directions (DC bus ↔ battery). This converter consists of four switches (S_1, S_2, S_3, S_4), two filter capacitors (bus capacitor, C_{bus}, with capacitance, C_{bus}, and battery capacitor, C_{bat}, with capacitance,

C_{bat}), and an inductor (L_1 with inductance L_1). In addition, it can transfer the energy of the DC bus (or battery) to the wireless charging load because L_1 also acts as a transmitting coil for WPT.

The AC-DC converter is connected to a wireless charging load, such as a cell phone or laptop, and it has a receiving coil (L_2 with inductance L_2) for WPT, a filter capacitor (WPT capacitor, C_{wpt}, with capacitance, C_{wpt}), a resonant capacitor (C_r with capacitance, C_r), and a voltage doubler rectifier that consists of two diodes (D_1, D_2) and two doubler capacitors (C_1 with capacitance, C_1, and C_2 with capacitance, C_2).

L_1 and L_2 are parts of the two-coil structure; they are coupled magnetically with a coupling coefficient, k, to transfer the energy wirelessly. Based on [19,20], the two-coil structure can be represented as a transformer with a leakage inductor (L_{lk} with inductance, L_{lk}), an effective turn ratio (N_e), and a magnetizing inductor (L_m with inductance, L_m), where $L_{lk} = (1-k^2)L_2$, $N_e = k\sqrt{L_2/L_1}$, and $L_m = L_1$ (Figure 2b).

Four switches achieve the ZVS turn-on by using the stored energy in L_1. L_{lk} resonates with C_r, and high voltage gain between the DC bus and wireless charging load is achieved by setting the switching frequency, f_S, to the resonant frequency, f_r, between L_{lk} and C_r. The voltage doubler rectifier converts AC voltage to DC voltage for wireless charging load, and clamps the reverse voltages of D_1 and D_2 to WPT voltage, V_{wpt}.

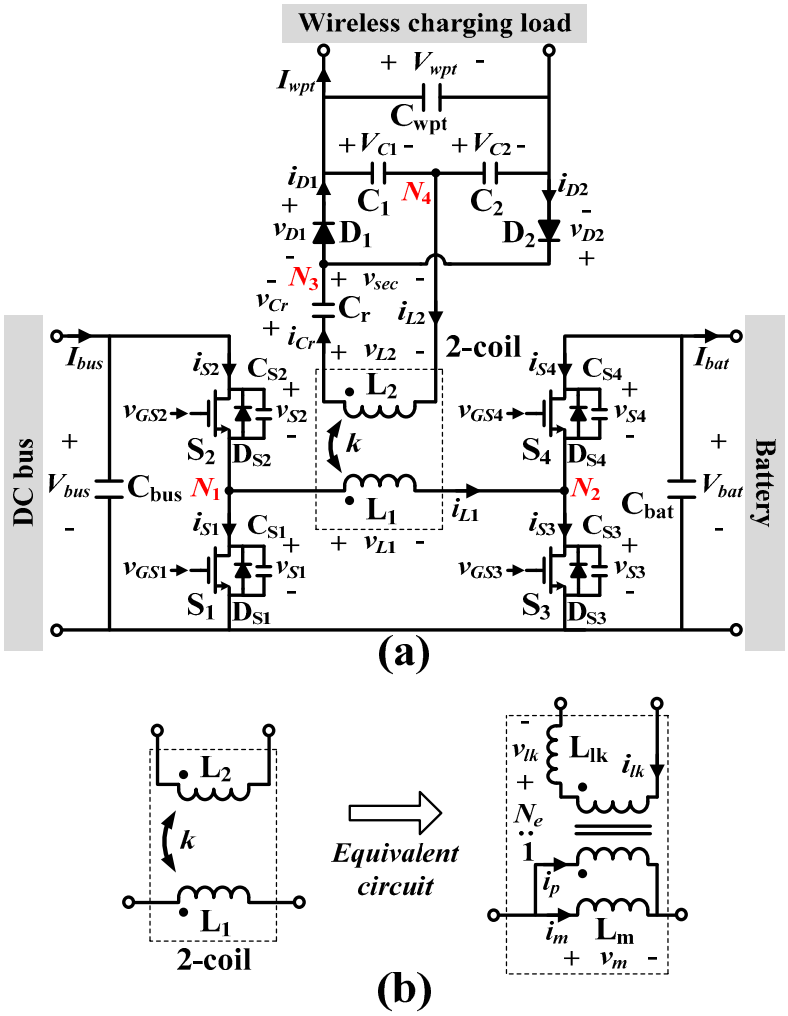

Figure 2. (**a**) Circuit structure of the proposed converter. (**b**) Equivalent circuit of the two-coil structure.

2.2. Principle of Operation

The proposed converter operates at a fixed switching frequency ($f_S = 1/T_S$), where T_S is a switching period, and it controls the voltage gain between the DC bus voltage, V_{bus}, and battery voltage, V_{bat}, by changing the duty ratios of S_1, S_2, S_3, and S_4; the duty ratios of S_2 and S_3 are defined as D, and the duty ratios of S_1 and S_4 are defined as 1–D. In addition, the voltage gain between V_{bus} and V_{wpt} is adjusted by using N_e.

The equivalent circuits (Figure 3) and operating waveforms (Figure 4) were obtained under the following assumptions and conditions: (1) All components are lossless, (2) C_1, C_2, C_{bus}, C_{bat}, and C_{wpt} are large enough to assume that V_{C1}, V_{C2}, V_{bus}, V_{bat}, and V_{wpt} are constant voltage sources, (3) $f_r = f_S$, and (4) the converter operates in a steady state. The converter operates in four modes.

Mode 1 (Figure 3a, $t_0 \le t \le t_1$): This mode starts at $t = t_0$ when S_2 and S_3 are turned on. At this time, S_2 and S_3 achieve ZVS turn-on because the body diodes, D_{S2} and D_{S3}, of S_2 and S_3 are turned on before $t = t_0$. During this mode, the voltage, v_m, of L_m becomes V_{bus}, and the current, i_m, of L_m is:

$$i_m(t) = i_m(t_0) + (V_{bus}/L_m)(t - t_0), \tag{1}$$

where $i_m(t_0) = I_{bus} + I_{bat} - V_{bus}DT_S/(2L_m)$. C_r has voltage $v_{Cr} = N_eV_{bus} - V_{C1}–v_{lk}$ and current $i_{Cr} = i_{lk}$, and $i_{Cr}(t_0) = 0$. Therefore:

$$i_{Cr}(t) = \frac{N_eV_{bus} - V_{wpt}/2 - v_{Cr}(t_0)}{\sqrt{L_{lk}/C_r}} \sin[\omega_r(t - t_0)], \tag{2}$$

where $v_{Cr}(t_0) = -0.5T_SI_{wpt}/C_r$ and $\omega_r = 1/\sqrt{L_{lk}C_r}$. The current, i_{D1}, of D_1 is equal to i_{Cr} for $t_0 \le t \le t_1$.

Mode 2 (Figure 3b, $t_1 \le t \le t_2$): At $t = t_1$, S_2 and S_3 are turned off, and S_1 and S_4 remain in the off-states to prevent a shoot-through problem. This mode is known as dead time. During this mode, the output capacitance, C_{S1}, of S_1 discharges from V_{bus} to 0, and the output capacitance, C_{S2}, of S_2 charges from 0 to V_{bus}. In addition, the output capacitance, C_{S4}, of S_4 discharges from V_{bat} to 0, and the output capacitance, C_{S3}, of S_3 charges from 0 to V_{bat}. Shortly after the discharging and charging processes are finished, the body diodes, D_{S1} and D_{S4}, of S_1 and S_4 are turned on.

Mode 3 (Figure 3c, $t_2 \le t \le t_3$): At $t = t_2$, S_1 and S_4 are turned on under ZVS conditions because the body diodes, D_{S1} and D_{S4}, are turned on before $t = t_2$. During this mode:

$$i_m(t) = i_m(t_2) - (V_{bat}/L_m)(t - t_2), \tag{3}$$

because $v_m = -V_{bat}$. i_{Cr} is obtained using $v_{Cr} = -N_eV_{bat} + V_{C2} - v_{lk}$ and $i_{Cr}(t_2) = 0$ as:

$$i_{Cr}(t) = -\frac{N_eV_{bat} - V_{wpt}/2 + v_{Cr}(t_2)}{\sqrt{L_{lk}/C_r}} \sin[\omega_r(t - t_2)], \tag{4}$$

where $v_{Cr}(t_2) = 0.5T_SI_{wpt}/C_r$. At $t = t_2$, D_2 is turned on, and the current, i_{D2}, of D_2 is $-i_{Cr}$.

Mode 4 (Figure 3d, $t_3 \le t \le t_4$): S_2 and S_3 remain in the off-states because this mode is the dead time interval. During this mode, C_{S2} discharges from V_{bus} to 0, and C_{S1} charges from 0 to V_{bus}. In addition, C_{S3} discharges from V_{bat} to 0, and C_{S4} charges from 0 to V_{bat}. Shortly after the discharging and charging processes are finished, D_{S2} and D_{S3} are turned on.

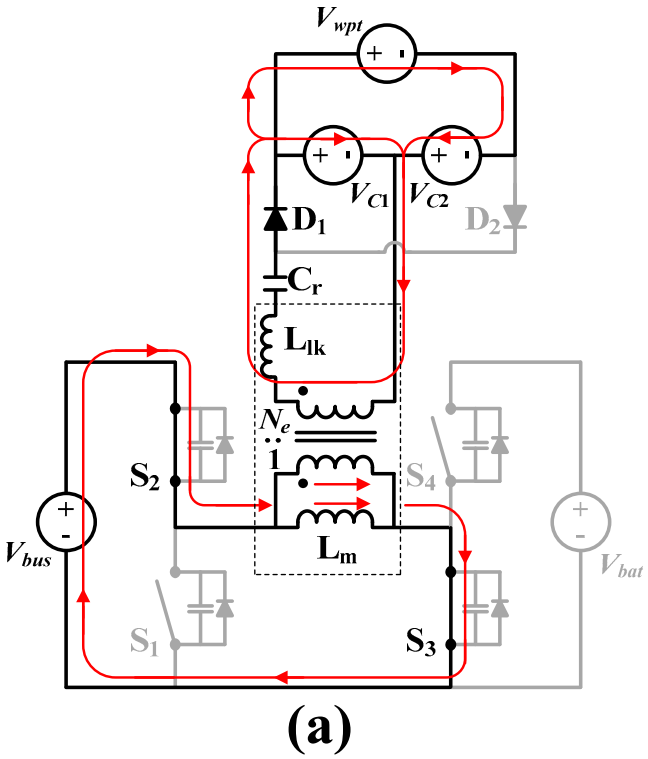

Figure 3. *Cont.*

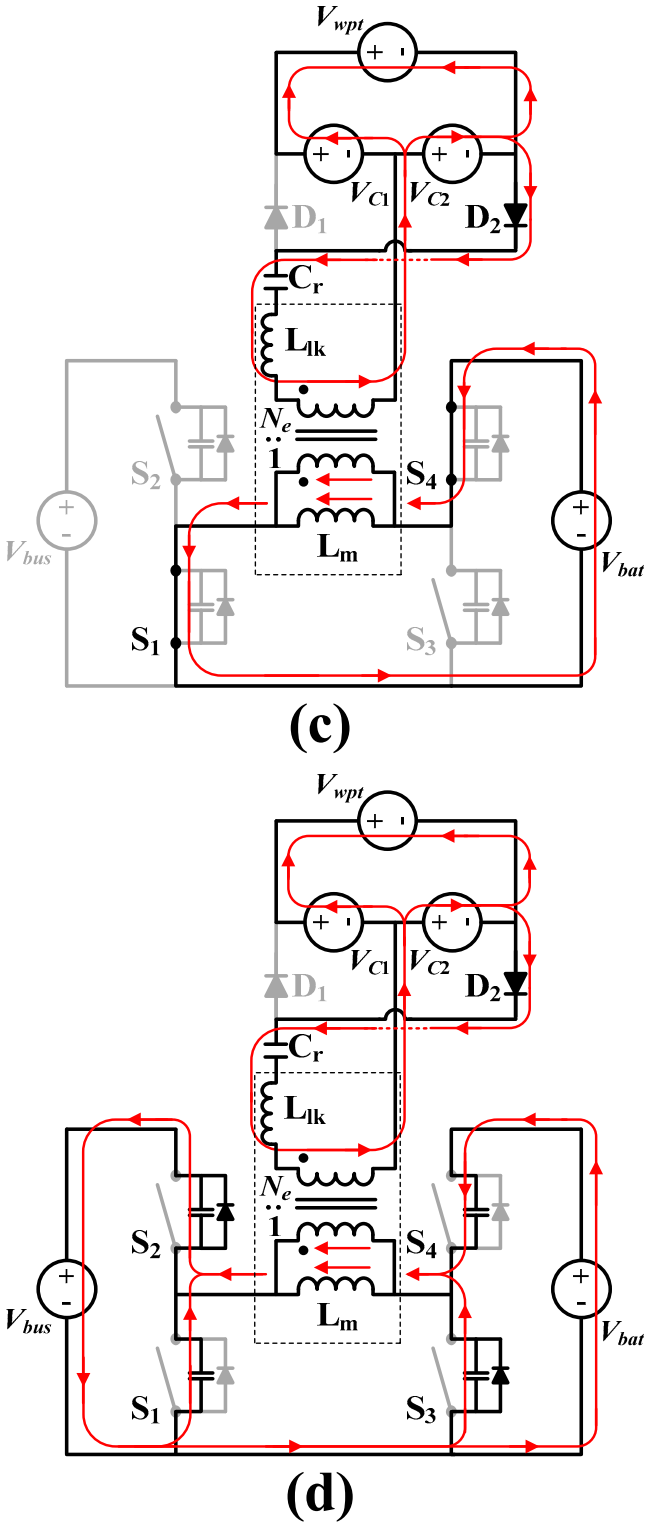

Figure 3. (**a**) Circuit diagrams for the operation in Mode 1. (**b**) Circuit diagrams for the operation in Mode 2. (**c**) Circuit diagrams for the operation in Mode 3. (**d**) Circuit diagrams for the operation in Mode 4.

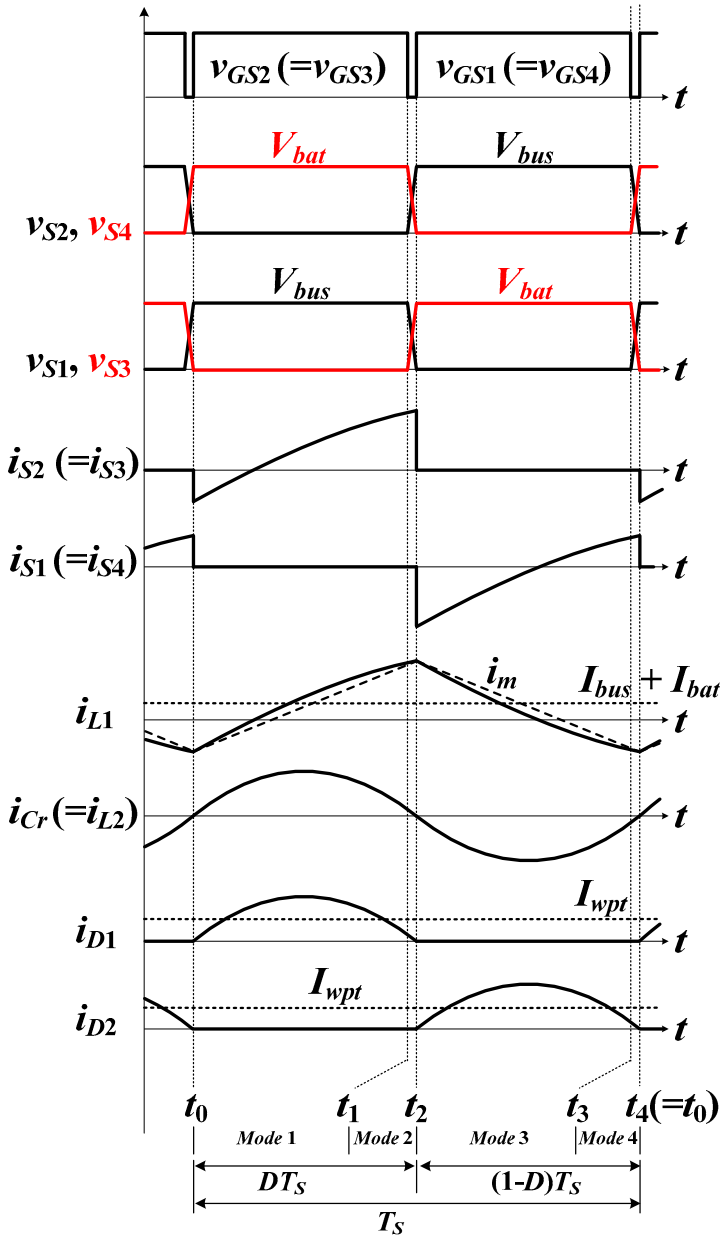

Figure 4. Operational waveforms of the proposed converter.

2.3. Voltage Gain

The proposed converter has one input port (DC bus) and two output ports (battery and wireless charging load). Therefore, it has (Equation (1)) a voltage gain, G_{bb}, between the DC bus and battery and (Equation (2)) a voltage gain, G_{wb}, between the DC bus and wireless charging load.

(1) $G_{bb} = V_{bat}/V_{bus}$

For one T_S, the average voltages of C_{bus} and C_{bat} are V_{bus} and V_{bat}, respectively. Then, the average voltage at node N_1 between S_1 and S_2 is DV_{bus}, and the average voltage at node N_2 between S_3 and S_4 is given by (1-D) V_{bat}. The average voltage of L_1 is zero due to the volt-second balance law for the inductor, and the average currents of switches are given by $<i_{S2}> = <i_{S3}> = I_{bus}$ and $<i_{S1}> = <i_{S4}> = -I_{bat}$ because the average current of the capacitor is zero by the charge balance law. Therefore, the average model of the circuit can be obtained (Figure 5). In this average model, the series resistance, R_S, is the sum of R_{L1} and $2R_{on}$, where R_{L1} and R_{on} are a winding resistance of L_1 and on-resistance of a switch, respectively.

By applying Kirchhoff's voltage law (KVL) to the closed-loop that contains DV_{bus}, R_S, and (1-D) V_{bat}, the voltage gain G_{bb} (= V_{bat}/V_{bus}) is obtained as:

$$G_{bb} = -\frac{1}{2}\left\{\left[\frac{(1-D)R_{bat}}{R_S}+1\right]+\sqrt{\left[\frac{(1-D)R_{bat}}{R_S}+1\right]^2+\frac{4DR_{bat}}{R_S}}\right\}, \quad (5)$$

where $R_{bat} = V_{bat}/I_{bat}$. In most cases, $R_{bat} >> R_S$, so:

$$G_{bb} \approx D/(1-D). \quad (6)$$

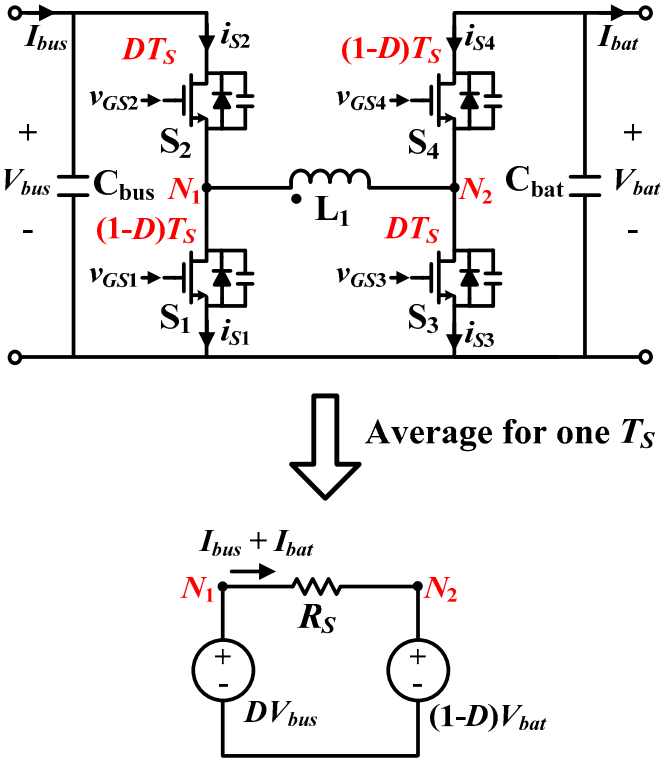

Figure 5. Average model between node N_1 and node N_2.

(2) $G_{wb} = V_{wpt}/V_{bus}$

Based on the four nodes (N_1, N_2, N_3, and N_4) in Figure 2a, the circuit of the proposed converter can be simplified (Figure 6a). Here, the square voltage, v_{ac}, between N_1 and N_2 is $V_{bus} - (I_{bus} + I_{bat})R_S$ for DT_S and $-V_{bat} - (I_{bus} + I_{bat})R_S$ for (1-D)T_S. Then, the current i_{ac} is $i_{L1} - (I_{bus} + I_{bat})$, and the square voltage, v_{ac2}, between N_3 and N_4 becomes $V_{wpt}/2$ for $0.5T_S$ and $-V_{wpt}/2$ for the other $0.5T_S$. The current i_{ac2} is given by i_{Cr}.

By applying fundamental harmonic approximation (FHA) to v_{ac}, i_{ac}, i_{ac2}, and v_{ac2}, the following root mean square (RMS) values are obtained (Figure 6b); $V_{L2,\mathrm{rms}}$ is the RMS value of the first harmonic component in the voltage, v_{L2}, of L_2, and it is given by:

$$V_{L2,rms} = -\frac{N_e{}^2\pi V_{wpt}R_S}{\sqrt{2}R_{wpt}} + \frac{N_eV_{bus}}{\sqrt{2}}\left(\frac{2(1+G_{bb})}{\pi}\sin(D\pi) - \frac{T_SR_S}{\pi^2(1-D)L_m}\right), \quad (7)$$

where:

$$I_{ac2,rms} = \pi I_{wpt}/\sqrt{2}, \quad (8)$$

and:

$$V_{ac2,rms} = \sqrt{2}V_{wpt}/\pi, \tag{9}$$

are RMS values of the first harmonic components in i_{ac2} and v_{ac2}, respectively. Then, the equivalent resistance, R_{ac2}, between N_3 and N_4 is obtained using Equations (8) and (9) as:

$$R_{ac2} = V_{ac2,rms}/I_{ac2,rms} = 2R_{wpt}/\pi^2, \tag{10}$$

where $R_{wpt} = V_{wpt}/I_{wpt}$. By applying KVL to the closed-loop in Figure 6b, the relation between $V_{L2,\mathrm{rms}}$ and $V_{ac2,\mathrm{rms}}$ is given by:

$$\frac{V_{L2,rms}}{V_{ac2,rms}} = \frac{1}{R_{ac2}}\left[j\left(\omega_S L_{lk} - \frac{1}{\omega_S C_r}\right) + R_{L2}\right] + 1, \tag{11}$$

where R_{L2} is a winding resistance of L_2. Then, substituting Equations (7) and (9) into Equation (11) yields:

$$\begin{aligned} G_{wb} = \left|\frac{V_{wpt}}{V_{bus}}\right| = \frac{N_e}{2}\left(2(1+G_{bb})\sin(D\pi) - \frac{T_S R_S}{\pi(1-D)L_m}\right) \\ \Big/ \sqrt{\frac{1}{{R_{ac2}}^2}\left(\omega_S L_{lk} - \frac{1}{\omega_S C_r}\right)^2 + \left(\frac{\pi^2 R_{L2}}{2R_{wpt}} + 1 + \frac{{N_e}^2\pi^2 R_S}{2R_{wpt}}\right)^2}. \end{aligned} \tag{12}$$

If $f_r = f_S$, maximum G_{wb} is obtained because $\omega_S L_{lk} = 1/(\omega_S C_r)$ at $f_r = f_S$ (Figure 7), and it is given by:

$$G_{wb}|_{f_r=f_S} = \frac{N_e}{2}\left(2(1+G_{bb})\sin(D\pi) - \frac{T_S R_S}{\pi(1-D)L_m}\right)\Big/\left(\frac{\pi^2 R_{L2}}{2R_{wpt}} + 1 + \frac{{N_e}^2\pi^2 R_S}{2R_{wpt}}\right). \tag{13}$$

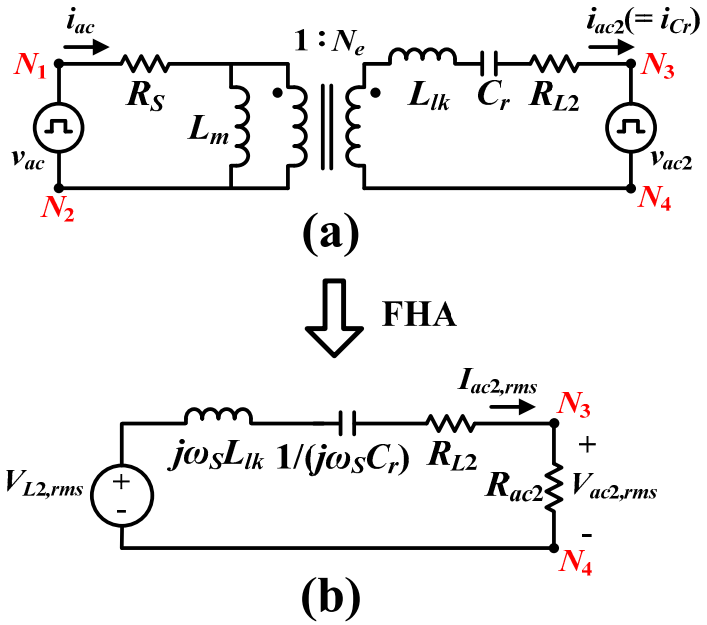

Figure 6. (**a**) Equivalent circuit based on four nodes (N_1, N_2, N_3, and N_4). (**b**) AC model in the secondary winding side after applying fundamental harmonic approximation (FHA).

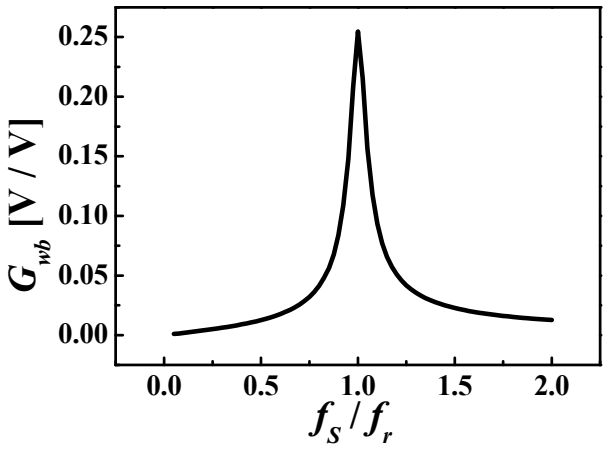

Figure 7. Voltage gain (G_{wb}) between V_{bus} and V_{wpt} according to f_S.

Therefore, C_r should be chosen to obtain the maximum voltage gain (G_{wb}) between V_{bus} and V_{wpt}. Because $\omega_r = 1/\sqrt{L_{lk}C_r}$ and $L_{lk} = (1-k^2)L_2$, C_r can be determined as:

$$C_r = \frac{1}{4\pi^2 {f_S}^2 (1-k^2) L_2}.$$

2.4. Magnetic Saturation

The coil structure, which consists of a transmitting coil (L_1) and a receiving coil (L_2), can use magnetic bars to increase efficiency and reduce magnetic fields that can interfere with nearby electronics [21–23]. Based on [24,25], the magnetic flux density (B_C) of the coil structure is given by:

$$B_C = \frac{\mu_0 \mu_e N i_{m,peak}}{l_m}, \tag{14}$$

where μ_0 is a vacuum permeability, $\mu_e = (\mu_r l_m)/\left(2l_g\mu_r + l_m\right)$ is an effective relative permeability, N is the number of turns, $i_{m,peak}$ is a peak value of i_m, l_m is the mean magnetic path length, μ_r is a relative permeability, and l_g is thee air-gap length.

Because the proposed converter has a DC bias current (=I_{bus} + I_{bat}) of L_1, $i_{m,peak}$ is given by:

$$i_{m,peak} = I_{bus} + I_{bat} + \frac{V_{bus} D T_S}{2L_m}. \tag{15}$$

Magnetic saturation can be caused by this DC bias current because the DC bias current increases B_C by increasing $i_{m,peak}$. There are two methods to solve the problem of the DC bias current [26,27]. First, decreasing N reduces B_C. Second, increasing l_g reduces B_C by decreasing μ_e. However, l_g is determined by a distance, l_d, between L_1 and L_2. Therefore, the following condition for preventing magnetic saturation can be obtained using $B_C < B_{sat}$, (Equations (14) and (15)) as:

$$N < \frac{l_m B_{sat}}{\mu_0 \mu_e [I_{bus} + I_{bat} + V_{bus} D T_S/(2L_m)]}, \tag{16}$$

where B_{sat} is a saturation flux density of magnetic material.

3. Experimental Results

A prototype (Figure 8) of the proposed converter was fabricated using selected components and circuit parameters (Table 1), then tested to verify the operation of the proposed converter.

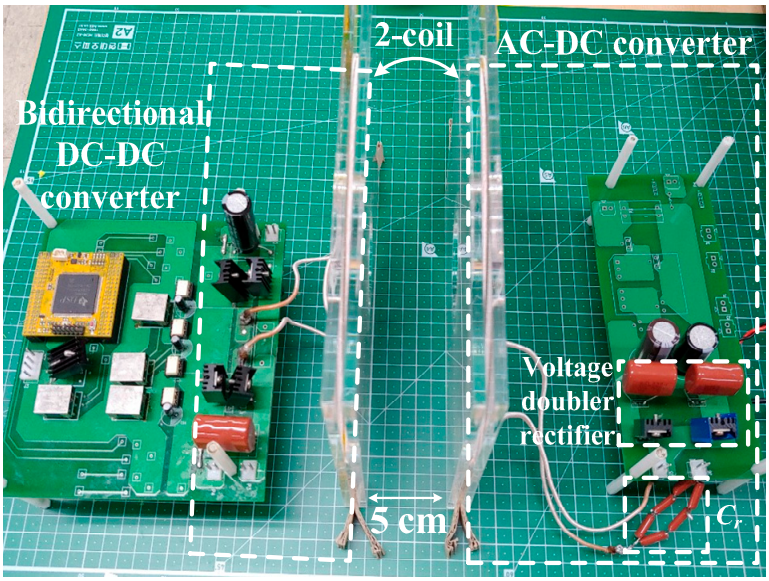

Figure 8. Photograph of the prototype.

Table 1. Values of the components used for the prototype.

Components			Values
2-coil structure	Winding type		Spiral
	Distance between two coils		5 cm
	Coupling coefficient (k)		0.227
	Equivalent turn ratio (N_e)		0.226
	Primary winding	Inductance (L_1)	117.5 μH
		Resistance (R_{L1})	0.43 Ω
		Turn number (N_1)	28 T
	Secondary winding	Inductance (L_2)	116.5 μH
		Resistance (R_{L2})	0.4 Ω
		Turn number (N_2)	28 T
Resonant capacitor (C_r)			1.43 nF
Doubler capacitors (C_1, C_2)			2.2 μF
Switches (S_1~S_4)			FCP099N60E (R_{on} = 99 mΩ)
Diodes (D_1, D_2)			BYV29-500

The voltage and current waveforms of S_1 and S_2 were measured at V_{bus} = 400 V, V_{bat} = 400 V, f_S = 400 kHz, and P_{wpt} (or P_{bat}) = 20 and 100 W (Figure 9). At both P_{wpt} = 20 W (Figure 9a) and P_{wpt} = 100 W (Figure 9b), the voltage stresses of S_1 and S_2 were measured as 400 V, which is equal to V_{bus}, and S_1 and S_2 achieved ZVS turn-on. In addition, S_3 and S_4 achieved ZVS turn-on at these conditions because $i_{S1} = i_{S4}$ and $i_{S2} = i_{S3}$. Even at both P_{bat} = 20 W (Figure 9c) and P_{bat} = 100 W (Figure 9d), all switches were turned on under the ZVS condition, which improves the power-conversion efficiency, η_e.

The theoretical V_{wpt} obtained from Equation (13) was compared with the experimental V_{wpt} measured at V_{bus} = 400 V, V_{bat} = 400 V, and P_{wpt} = 20 W~100 W (Figure 10). The theoretical V_{wpt} was higher than experimental V_{wpt} at all P_{wpt}, but the difference was <3%. This result shows that Equation (13) predicts the experimental V_{wpt} with little error. In addition, V_{wpt} was almost constant regardless of P_{wpt}.

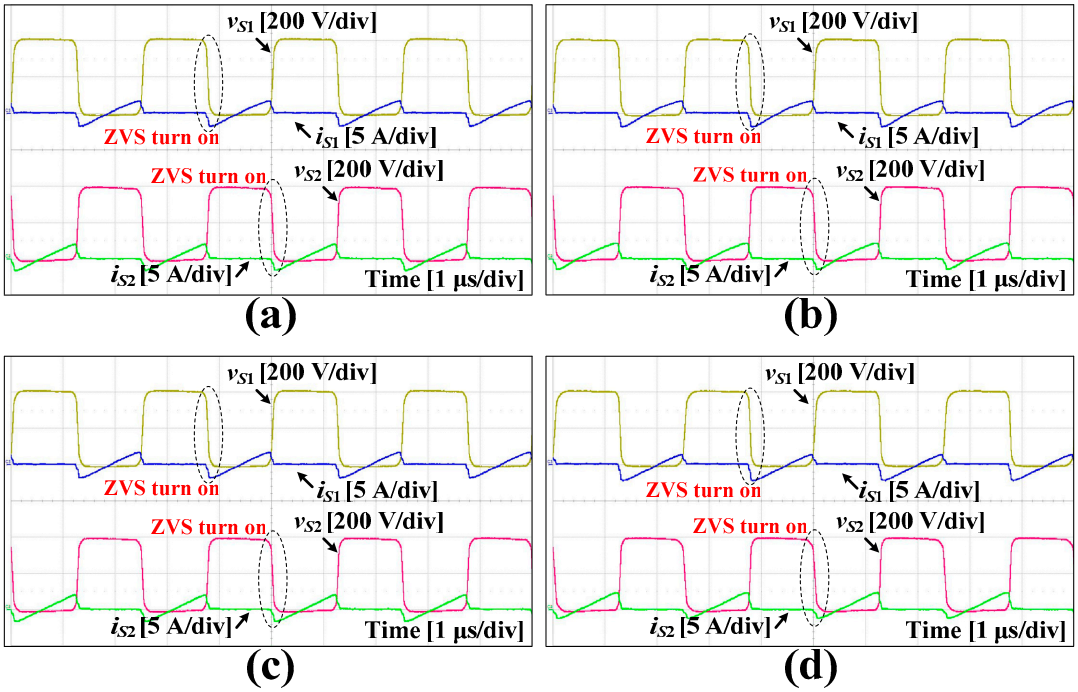

Figure 9. Voltage and current waveforms of switches (S_1, S_2) measured at P_{wpt} = (**a**) 20 W and (**b**) 100 W or at P_{bat} = (**c**) 20 and (**d**) 100 W.

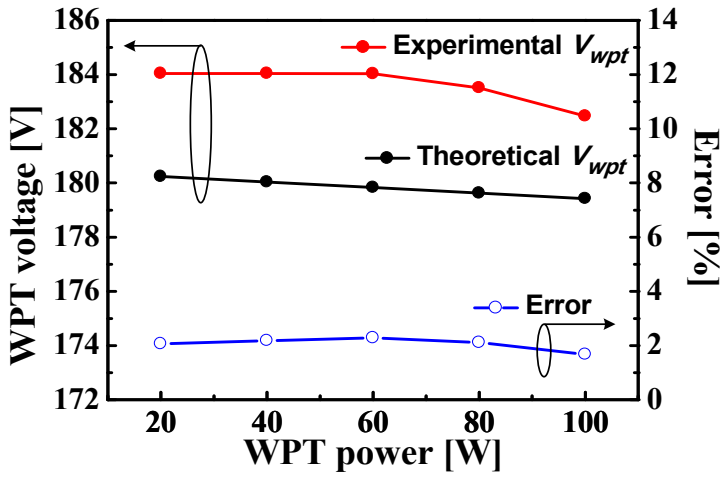

Figure 10. Comparison between experimental V_{wpt} and theoretical V_{wpt}.

The power-conversion efficiencies ($\eta_{e,\mathrm{wpt}}$ for the wireless charging load and $\eta_{e,\mathrm{bat}}$ for the battery load) were measured at V_{bus} = 400 V, V_{bat} = 400 V, f_S = 400 kHz, and P_{wpt} (or P_{bat}) = 20 W~100 W (Figure 11). The proposed converter had the highest $\eta_{e,\mathrm{wpt}}$ = 93.8% at P_{wpt} = 100 W (Figure 11a) and had the highest $\eta_{e,\mathrm{bat}}$ = 95.9% at P_{bat} = 100 W (Figure 11b). At low P_{wpt} = 20 W, the measured $\eta_{e,\mathrm{wpt}}$ was 82.5% (Figure 11a), and the measured $\eta_{e,\mathrm{bat}}$ was 83.5% at low P_{bat} = 20 W (Figure 11b). In addition, the measured $\eta_{e,\mathrm{bat}}$ was higher than the measured $\eta_{e,\mathrm{wpt}}$ because the wireless power loss during transfer between two coils is included in $\eta_{e,\mathrm{wpt}}$. These results show that the proposed converter had high $\eta_{e,\mathrm{wpt}}$ > 82% and high $\eta_{e,\mathrm{bat}}$ > 83% for all operating ranges due to the ZVS turn-on of all switches.

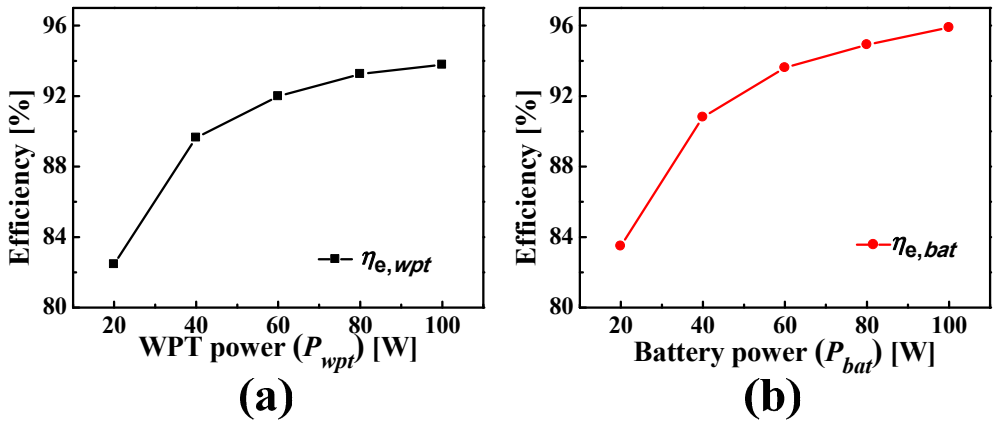

Figure 11. (**a**) Power-conversion efficiency, $\eta_{e,\mathrm{wpt}}$, measured at P_{wpt} = 20 W~100 W. (**b**) Power-conversion efficiency, $\eta_{e,\mathrm{bat}}$, measured at P_{bat} = 20 W~100 W.

The transient response of V_{wpt} was measured at V_{bus} = 400 V, V_{bat} = 400 V, and f_S = 400 kHz, while changing the wireless charging load from 20% to 100% and from 100% to 20% (Figure 12). At the load transition, the maximum voltage spike of V_{wpt} was measured as 14 $V_{p.p}$, and V_{wpt} returned to the steady-state within 81 ms.

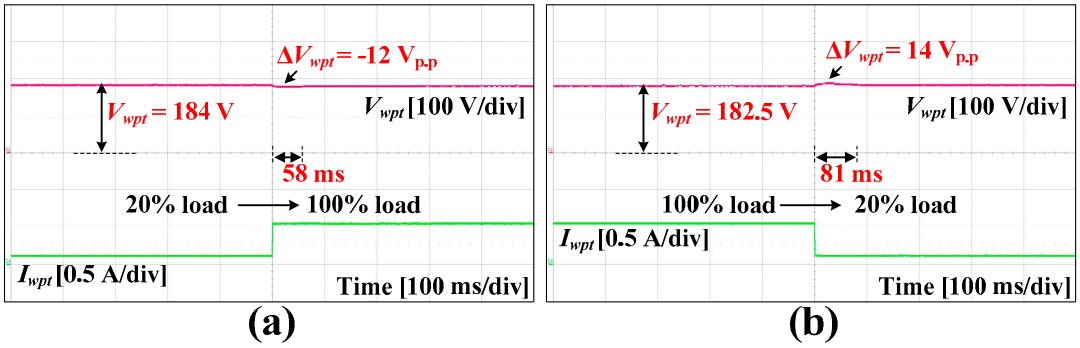

Figure 12. Transient responses of V_{wpt} while changing the wireless charging load (**a**) from 20% to 100% and (**b**) from 100% to 20%.

In addition, the transient response of V_{bat} was measured while changing the battery load from 20% to 100% and from 100% to 20% under the same conditions as in Figure 12 (Figure 13). The maximum voltage spike of V_{bat} was measured as 61 $V_{p.p}$ when the load changed, and V_{bat} returned to the steady state within 125 ms. These experiment results of the transient response show that the proposed converter can operate properly despite sudden load changes.

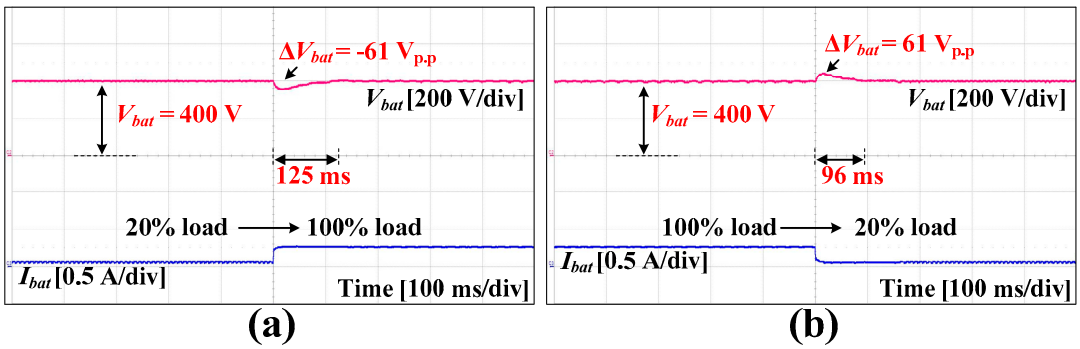

Figure 13. Transient responses of V_{bat} while changing the battery load (**a**) from 20% to 100% and (**b**) from 100% to 20%.

To show that the proposed converter can operate both when charging the battery and when charging wirelessly, V_{wpt} and V_{bat} of the proposed converter were measured under the following four conditions (Figure 14): (1) P_{wpt} = 20 W and P_{bat} = 20 W, (2) P_{wpt} = 20 W and P_{bat} = 100 W, (3) P_{wpt} = 100 W and P_{bat} = 20 W, and (4) P_{wpt} = 100 W and P_{bat} = 100 W. Figure 14 shows that V_{wpt} decreases and V_{bat} increases when the power (P_{wpt}, P_{bat}) increases. However, both V_{wpt} and V_{bat} maintained a near fixed value; V_{wpt} changed from 183.8 to 180.9 V, which is just a 1.58% change, and V_{bat} changed from 399.8 to 401 V, which is just a 0.3% change.

The measured V_{wpt} and V_{bat} are summarized in Table 2, and this experimental result shows that the proposed converter can operate in both charging the battery and charging wirelessly because both V_{wpt} and V_{bat} maintain a near fixed value regardless of P_{wpt} and P_{bat}.

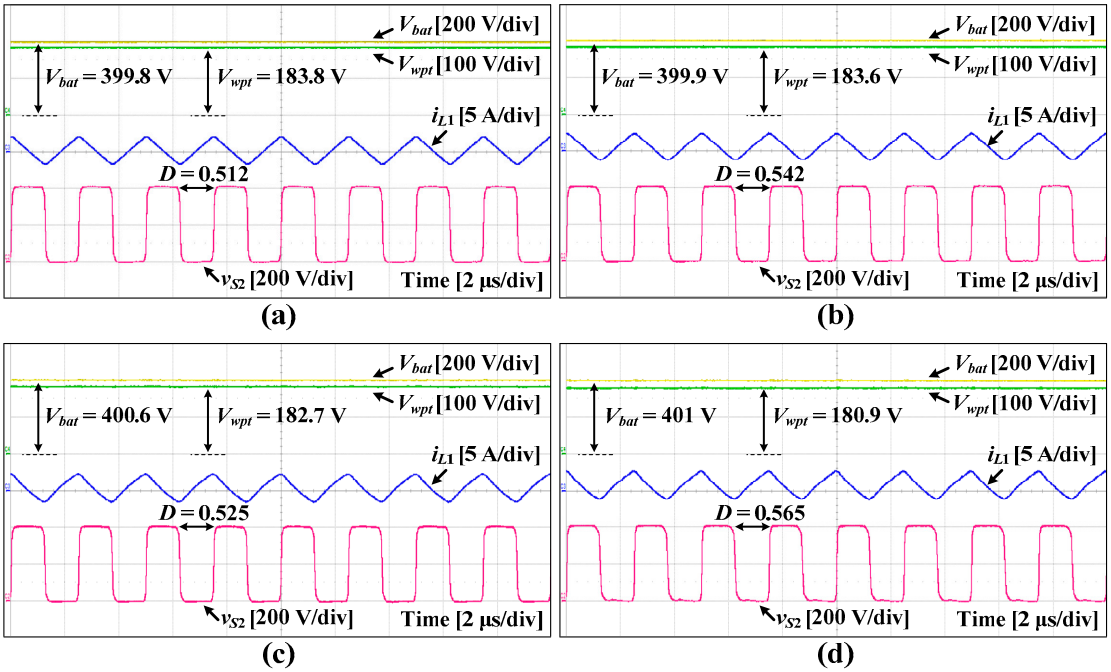

Figure 14. The WPT voltage (V_{wpt}) and the battery voltage (V_{bat}) measured at (**a**) P_{wpt} = 20 W and P_{bat} = 20 W, (**b**) P_{wpt} = 20 W and P_{bat} = 100 W, (**c**) P_{wpt} = 100 W and P_{bat} = 20 W, and (**d**) P_{wpt} = 100 W and P_{bat} = 100 W.

Table 2. WPT and battery voltages according to the WPT and battery powers.

Power	WPT Power (P_{wpt}) / Battery Power (P_{wpt})	20 W / 20 W	20 W / 100 W	100 W / 20 W	100 W / 100 W
	WPT voltage (V_{wpt})	183.8 V	183.6 V	182.7 V	180.9 V
	Battery voltage (V_{bat})	399.8 V	399.9 V	400.6 V	401 V

4. Conclusions

This paper presented a three-port converter to integrate an ES system with a WPT system. If the ES and WPT systems are used separately, many converters are needed. However, these ES and WPT systems can be integrated through only one proposed converter because the proposed converter can use an inductor in the bidirectional DC-DC converter as a transmitting coil for the WPT system. Therefore, the proposed converter consists only of a bidirectional DC-DC converter and an AC-DC converter, and an ES-WPT system that uses the proposed converter can minimize the cost and circuit size. The operation of the proposed converter was verified by theoretical analysis and experimental results, and the proposed converter had high $\eta_{e,\mathrm{wpt}} > 82\%$ for 20 W $\leq P_{wpt} \leq$ 100 W, and $\eta_{e,\mathrm{bat}} > 83\%$ for 20 W $\leq P_{bat} \leq$ 100 W, due to the ZVS turn-on of all switches. These results show that the proposed

converter is suitable for the ES-WPT system that is part of future PV energy delivery and management infrastructure for residential applications.

Author Contributions: Both authors contributed equally to this work. H.-S.L. presented the main idea of the three-port converter. H.-S.L. and J.-J.Y. analyzed the proposed converter and performed experiments. J.-J.Y. contributed to the overall composition and writing of the manuscript. All authors have read and agreed to the published version of the manuscript.

Funding: This work was supported by the National Research Foundation of Korea (NRF) grant funded by the government of Korea (MSIP) (NRF-2018R1A1A1A05079496).

Conflicts of Interest: The authors have no conflict of interest.

References

1. Malinowski, M.; Leon, J.I.; Abu-Rub, H. Solar photovoltaic and thermal energy systems: Current technology and future trends. *Proc. IEEE* **2017**, *105*, 2132–2146. [CrossRef]
2. Kroposki, B.; Johnson, B.; Zhang, Y.; Gevorgian, V.; Denholm, P.; Hodge, B.-M.; Hannegan, B. Achieving a 100% renewable grid: Operating electric power systems with extremely high levels of variable renewable energy. *IEEE Power Energy Mag.* **2017**, *15*, 61–73. [CrossRef]
3. Sahu, B.K. A study on global solar PV energy developments and policies with special focus on the top ten solar PV power producing countries. *Renew. Sustain. Energy Rev.* **2015**, *43*, 621–634. [CrossRef]
4. McElroy, M.B.; Chen, X. Wind and solar power in the United States: Status and prospects. *CSEE J. Power Energy Syst.* **2017**, *3*, 1–6. [CrossRef]
5. Park, L.; Jang, Y.; Cho, S.; Kim, J. Residential Demand Response for Renewable Energy Resources in Smart Grid Systems. *IEEE Trans. Ind. Inf.* **2017**, *13*, 3165–3173. [CrossRef]
6. Chaudhari, K.; Ukil, A.; Kumar, K.N.; Manandhar, U.; Kollimalla, S.K. Hybrid Optimization for Economic Deployment of ESS in PV-Integrated EV Charging Stations. *IEEE Trans. Ind. Inf.* **2018**, *14*, 106–116. [CrossRef]
7. Liu, X.; Aichhorn, A.; Liu, L.; Li, H. Coordinated Control of Distributed Energy Storage System with Tap Changer Transformers for Voltage Rise Mitigation Under High Photovoltaic Penetration. *IEEE Trans. Smart Grid* **2012**, *3*, 897–906. [CrossRef]
8. Park, J.; Kim, D.; Hwang, K.; Park, H.H.; Kwak, S.I.; Kwon, J.H.; Ahn, S. A Resonant Reactive Shielding for Planar Wireless Power Transfer System in Smartphone Application. *IEEE Trans. Electromagn. Compat.* **2017**, *59*, 695–703. [CrossRef]
9. Jeong, N.S.; Carobolante, F. Enabling Wireless Power Transfer Though a Metal Encased Handheld Device. In Proceedings of the IEEE Wireless Power Transfer Conference, Aveiro, Portugal, 5–6 May 2016.
10. Nguyen, V.T.; Kang, S.H.; Choi, J.H.; Jung, C.W. Magnetic Resonance Wireless Power Transfer using Three-Coil System with Single Planar Receiver for Laptop Applications. *IEEE Trans. Consum. Electron.* **2015**, *61*, 160–166. [CrossRef]
11. Barman, S.D.; Reza, A.W.; Kumar, N.; Karim, M.E.; Munir, A.B. Wireless powering by magnetic resonant coupling: Recent trends in wireless power transfer system and its applications. *Renew. Sustain. Energy Rev.* **2015**, *51*, 1525–1552. [CrossRef]
12. Chen, Y.M.; Huang, A.Q.; Yu, X. A High Step-Up Three-Port DC–DC Converter for Stand-Alone PV/Battery Power Systems. *IEEE Trans. Power Electron.* **2013**, *28*, 5049–5062. [CrossRef]
13. Phattanasak, M.; Gavagsaz-Ghoachani, R.; Martin, J.P.; Nahid-Mobarakeh, B.; Pierfederici, S.; Davat, B. Control of a Hybrid Energy Source Comprising a Fuel Cell and Two Storage Devices Using Isolated Three-Port Bidirectional DC–DC Converters. *IEEE Trans. Ind. Appl.* **2015**, *51*, 491–497. [CrossRef]
14. Wang, P.; Lu, X.; Wang, W.; Xu, D. Frequency Division Based Coordinated Control of Three-Port Converter Interfaced Hybrid Energy Storage Systems in Autonomous DC Microgrids. *IEEE Access* **2018**, *6*, 25389–25398. [CrossRef]
15. Duarte, J.L.; Hendrix, M.; Simoes, M.G. Three-Port Bidirectional Converter for Hybrid Fuel Cell Systems. *IEEE Trans. Power Electron.* **2007**, *22*, 480–487. [CrossRef]
16. Wang, Z.; Li, H. An Integrated Three-Port Bidirectional DC–DC Converter for PV Application on a DC Distribution System. *IEEE Trans. Power Electron.* **2013**, *28*, 4612–4624. [CrossRef]

17. Mira, M.C.; Zhang, Z.; Knott, A.; Andersen, M.A.E. Analysis, Design, Modeling, and Control of an Interleaved-Boost Full-Bridge Three-Port Converter for Hybrid Renewable Energy Systems. *IEEE Trans. Power Electron.* **2017**, *32*, 1138–1155. [CrossRef]
18. Zhang, J.; Wu, H.; Qin, X.; Xing, Y. PWM Plus Secondary-Side Phase-Shift Controlled Soft-Switching Full-Bridge Three-Port Converter for Renewable Power Systems. *IEEE Trans. Ind. Electron.* **2015**, *62*, 7061–7072. [CrossRef]
19. Hesterman, B. Analysis and Modeling of Magnetic Coupling. Denver Chapter, IEEE Power Electronics Society. 2007, pp. 35–38. Available online: http://www.verimod.com/presentations/Denver_PELS_20070410_Hesterman_Magnetic_Coupling.pdf (accessed on 16 December 2019).
20. Zhu, G.; McDonald, B.A.; Wang, K. Modeling and Analysis of Coupled Inductors in Power Converters. *IEEE Trans. Power Electron.* **2011**, *26*, 1355–1363. [CrossRef]
21. Dai, J.; Ludois, D.C. A Survey of Wireless Power Transfer and a Critical Comparison of Inductive and Capacitive Coupling for Small Gap Applications. *IEEE Trans. Power Electron.* **2015**, *30*, 6017–6029. [CrossRef]
22. Xu, H.; Wang, C.; Xia, D.; Liu, Y. Design of Magnetic Coupler for Wireless Power Transfer. *Energies* **2019**, *12*, 3000. [CrossRef]
23. Dayerizadeh, A.; Lukic, S. Saturable inductors for superior reflexive field containment in inductive power transfer systems. In Proceedings of the IEEE Applied Power Electronics Conference and Exposition (APEC), San Antonio, TX, USA, 4–8 March 2018.
24. McLyman, W.T. *Transformer and Inductor Design Handbook*, 3rd ed.; Marcel Dekker, Inc.: New York, NY, USA, 2004.
25. Mohan, N.; Undeland, T.M. *Power Electronics: Converters, Applications, and Design*; John Wiley & Sons: Hoboken, NJ, USA, 2007.
26. Orenchak, G.G. Specify Saturation Properties of Ferrite Cores to Prevent Field Failure. Available online: http://www.tscinternational.com/tech13.pdf (accessed on 16 December 2019).
27. Itoh, Y.; Hattori, F.; Kimura, S.; Imaoka, J.; Yamamoto, M. Design method considering magnetic saturation issue of coupled inductor in interleaved CCM boost PFC converter. In Proceedings of the IEEE Energy Conversion Congress and Exposition (ECCE), Montreal, QC, Canada, 20–24 September 2015.